

Notice: This manuscript has been authored by UT-Batelle, LLC, under contract DE-AC05-00OR22725 with the US Department of Energy (DOE). The US government retains and the publisher, by accepting the article for publication, acknowledges that the US government retains a nonexclusive, paid-up, irrevocable, worldwide license to publish or reproduce the published form of this manuscript, or allow others to do so, for US government purposes. DOE will provide public access to these results of federally sponsored research in accordance with the DOE Public Access Plan (<http://energy.gov/downloads/doe-public-access-plan>).

# Crystal field Hamiltonian and anisotropy in $\text{KErSe}_2$ and $\text{CsErSe}_2$

A. Scheie,<sup>1,\*</sup> V. O. Garlea,<sup>1</sup> L. D. Sanjeeva,<sup>2</sup> J. Xing,<sup>2</sup> and A. S. Sefat<sup>2</sup>

<sup>1</sup>*Neutron Scattering Division, Oak Ridge National Laboratory, Oak Ridge, Tennessee 37831, USA*

<sup>2</sup>*Materials Science and Technology Division, Oak Ridge National Laboratory, Oak Ridge, Tennessee 37831, USA*

(Dated: March 22, 2022)

We use neutron scattering and bulk property measurements to determine the single-ion crystal-field Hamiltonians of delafossites  $\text{KErSe}_2$  and  $\text{CsErSe}_2$ . Our analysis shows both to have an easy-plane ground state doublet with large  $J_z = 1/2$  terms and the potential for significant quantum effects, making them candidates for quantum spin liquid or other exotic ground states. We also show that inelastic neutron data and powder susceptibility alone cannot fully determine the Hamiltonians: two models emerge from the fits which match the data but which have opposite anisotropies. In this case, single-crystal directional magnetization or finite-field neutron scattering is necessary to identify the correct CEF Hamiltonian.

## I. INTRODUCTION

The triangular lattice is a canonical geometry in theories of quantum spin liquids (QSL), wherein spins are entangled in a long-range fluctuating ground state with fractionalized excitations [1–3]. Although isotropic quantum spins on a 2D triangular lattice order magnetically [4, 5], further neighbor exchange [6, 7] and magnetic anisotropy [8, 9] can theoretically produce a QSL state. Because magnetic anisotropy is driven by spin-orbit interactions,  $f$ -electron rare-earth ions are prime candidates for triangular-lattice QSLs [10–12]. One of the most prominent rare-earth triangular lattice QSL candidates has been  $\text{YbMgGaO}_4$  [13–17], although disorder-driven glassiness in the ground state casts doubt on the QSL hypothesis [18–22]. Nevertheless, since the discovery of  $\text{YbMgGaO}_4$  there has been a salvo of rare-earth based triangular lattice QSL candidates [23–29]. Any exotic behavior in these materials is heavily dependent upon magnetic anisotropy, so understanding the magnetic anisotropy is of key importance.

Magnetic single-ion anisotropy of an ion comes from crystal electric field (CEF) interactions with surrounding ligands [30, 31]. The CEF Hamiltonian also determines the ease of quantum tunnelling of the effective spin ground state: a system with strong quantum tunnelling effects will have large  $|J_z = \pm 1/2\rangle$  coefficients in its ground state [32]. Transitions between CEF levels are visible in neutron scattering, which allows the CEF parameters to be fitted to the energies and intensities of these modes [33].

Recently, a new family of rare-earth delafossite triangular lattice magnetic materials was reported based on the  $AB\text{Se}_2$  formula, where  $A$  is an alkali ion and  $B$  is a rare-earth ion [34, 35]. The whole series is triangular, but some of the compounds crystallize in the  $R\bar{3}m$  space group while others crystallize in the  $P6_3/mmc$  space group. This difference is in the stacking of triangular lattice layers, but it may also lead to subtle dif-

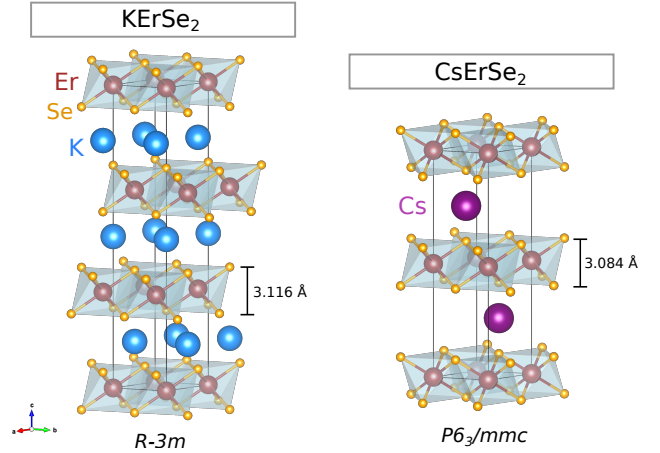


Figure 1. Crystal structures of  $\text{KErSe}_2$  (left) and  $\text{CsErSe}_2$  (right), showing the different stacking of triangular Er lattices. The  $\text{CsErSe}_2$  Se octahedra are slightly compressed along the  $c$  axis compared to  $\text{KErSe}_2$ .

ferences in magnetic anisotropy. In this study, we use inelastic neutron scattering and magnetization to determine the magnetic anisotropy of  $\text{Er}^{3+}$  triangular lattice materials  $\text{KErSe}_2$  ( $R\bar{3}m$ ) [35] and  $\text{CsErSe}_2$  ( $P6_3/mmc$ ) [34], shown in Fig. 1. Both of these compounds show no magnetic order or spin freezing down to 0.42 K, and single-crystal magnetization shows an easy-plane magnetic anisotropy with low-field magnetization indicating a correlated magnetic state in  $\text{KErSe}_2$  [35]. For rare-earths, an easy-plane anisotropy often indicates an effective  $|J_z = \pm 1/2\rangle$  ground state which allows for significant quantum effects. This, combined with the observed correlations and absence of magnetic order, makes these materials candidates for exotic magnetic behavior—possibly the spin liquid phase. Our analysis confirms that the ground state doublet has a large  $J_z = 1/2$  contribution with the potential for appreciable quantum effects. We also show that the CEF fit for these materials is underdetermined with zero-field neutron data and powder susceptibility data. Fully determining the CEF Hamiltonian requires bulk single crystal data or in-field neutron scat-

\* [scheieao@ornl.gov](mailto:scheieao@ornl.gov)

tering.

## II. EXPERIMENTS AND RESULTS

Powder samples of KErSe<sub>2</sub> and CsErSe<sub>2</sub> were synthesized in accord with refs. [35] and [34], respectively. We performed neutron scattering experiments using the HYSPEC instrument at the ORNL Spallation Neutron Source. Both KErSe<sub>2</sub> and CsErSe<sub>2</sub> samples weighting approximately 3 grams were loaded in a loose powder form inside 9.5 mm diameter Aluminum cans. We measured the KErSe<sub>2</sub> spectrum at 1.8 K, 15 K, 50 K and 100 K temperatures for 8 hours each with an incident neutron energy  $E_i = 9$  meV and Fermi chopper frequency of 360 Hz. Additional measurements were carried out at the same temperatures using  $E_i = 20$  meV. The sample was cooled down using a standard 100mm bore Orange cryostat. For the CsErSe<sub>2</sub> compound, we collected data at  $T = 1.8$  K and  $T = 50$  K for 7.5 hours using  $E_i = 9$  meV and 360 Hz. Further measurements were carried out using  $E_i = 30$  meV at 1.8 K. This sample was mounted and cooled in a vertical field cryomagnet. Measurements of CsErSe<sub>2</sub> under applied magnetic fields of up to 5 Tesla were performed to evaluate the Zeeman splitting of crystal field levels. The zero-field  $E_i = 9$  meV data for both compounds is shown in Fig. 2.

We also measured the powder-average susceptibility at 1 T between 2 K and 300 K and single crystal magnetization at 2 K using a Quantum Design MPMS. For the single-crystal measurements, 0.56 mg (KErSe<sub>2</sub>) and 1.75 mg (CsErSe<sub>2</sub>) plate-like crystals were used, with field oriented along the  $c$  axis (orthogonal to the plate surface) and then with field oriented in the  $ab$  plane (parallel to the plate surface). This data is shown in Fig. 4.

The neutron scattering spectra from KErSe<sub>2</sub> and CsErSe<sub>2</sub> (Fig. 2) show clear CEF transitions in both compounds. At 1.8 K, KErSe<sub>2</sub> has four visible modes at 0.731(8) meV, 3.34(1) meV, 5.10(2) meV, and 5.38(3) meV. Additional scans with  $E_i = 20$  meV revealed no additional peaks up to  $\hbar\omega = 19$  meV. Meanwhile, CsErSe<sub>2</sub> has four visible modes at 0.915(6) meV, 3.504(9) meV, 5.15(1) meV, and 5.56(1) meV. Additional scans with  $E_i = 30$  meV revealed no additional peaks up to  $\hbar\omega = 29$  meV (see Fig. 6). At higher temperatures, the low-energy modes become populated and many more transitions are visible in the neutron spectrum.

Low-temperature magnetization in Fig. 4 shows that both KErSe<sub>2</sub> and CsErSe<sub>2</sub> are more easily magnetized along the in-plane direction than in the  $c$  direction, indicating an easy-plane magnetic anisotropy. The close correspondence between the experimental data for these compounds suggests that the CEF Hamiltonians of these two compounds are very similar. The challenge is fitting the data to the appropriate model.

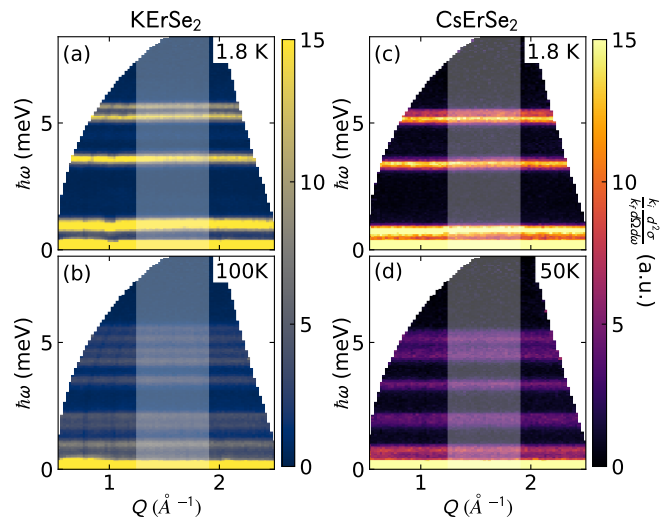


Figure 2. Powder neutron spectrum of KErSe<sub>2</sub> at 1.8 K (a) and 100 K (b), and CsErSe<sub>2</sub> at 1.8 K (c) and 50 K (d). The crystal field excitations are clearly visible. The grey region shows the  $Q$  range used to fit the CEF Hamiltonian.

## III. CEF ANALYSIS

The CEF Hamiltonian can be expressed using the Stevens Operator formalism as

$$\mathcal{H}_{CEF} = \sum_{n,m} B_n^m O_n^m. \quad (1)$$

Here  $O_n^m$  are the Stevens Operators [30, 36] and  $B_n^m$  are multiplicative factors called CEF parameters. Er<sup>3+</sup> is a Kramers ion with an effective spin  $J = 15/2$ , so up to eight doublet eigenstates will exist. For both KErSe<sub>2</sub> and CsErSe<sub>2</sub>, the Er<sup>3+</sup> ion has a  $D_3$  symmetric ligand environment with a rotation axis about  $c$ . Setting the  $z$  axis along  $c$ , symmetry dictates that only six CEF parameters are nonzero:  $B_2^0$ ,  $B_4^0$ ,  $B_4^3$ ,  $B_6^0$ ,  $B_6^3$ , and  $B_6^6$  [30]. These coefficients, once properly fitted to the data, uniquely define the CEF Hamiltonian.

To simplify the neutron data for the CEF fit, we integrated over  $1.25 \text{ \AA}^{-1} < Q < 1.9 \text{ \AA}^{-1}$  to create 2D data sets, shown in Fig. 3. This range was chosen to maximize the energy transfer range over which a consistent  $Q$  range is integrated. Given that the CEF excitations are local and have no dispersion, no information is lost by doing this. For KErSe<sub>2</sub>, we simultaneously fit the CEF model to the 1.8 K, 15 K, and 100 K data. For CsErSe<sub>2</sub>, we simultaneously fit the CEF model to the 1.8 K and 50 K data.

We fit the CEF Hamiltonian by minimizing the difference between the simulated and measured neutron spectra, rather than extracting peak energies and intensities beforehand. Thus we avoid making assumptions about overlapping peaks in the high-temperature data sets. For both KErSe<sub>2</sub> and CsErSe<sub>2</sub>, we defined the starting parameters with a point-charge model wherein surrounding

ligands are modeled as electrostatic point-charges [30] using PyCrystalField software [37]. We then fit the effective positions of the ligands to the neutron data, and then used the CEF parameters from that intermediate fit as starting values for fitting the CEF parameters directly. Details of the fitting procedure are in Appendix B.

The initial fitted CEF Hamiltonians yielded excellent matches to the neutron scattering data, but we found two different models which fit the KErSe<sub>2</sub> and CsErSe<sub>2</sub> neutron scattering data. One model shows an easy-plane ground state with  $B_2^0 < 0$ , the other shows an easy-axis ground state with  $B_2^0 > 0$ , with small variations between each material in the CEF parameters. The easy-plane model we call *Model 1* and the easy-axis model we call *Model 2*. Both Model 1 and Model 2 fits are shown in Fig. 3. (The overall  $\chi_{red}^2$  is larger for KErSe<sub>2</sub> than CsErSe<sub>2</sub>, possibly because of the more sophisticated background modeling used for CsErSe<sub>2</sub>.)

Despite the fact that Model 1 and Model 2 have completely different anisotropies, the calculated CEF spectra for both compounds are nearly identical and fit the neutron data beautifully. The reduced  $\chi^2$  for KErSe<sub>2</sub> is slightly lower for Model 2 ( $\chi_{redM1}^2 = 31.9$  vs  $\chi_{redM2}^2 = 29.8$ ), while reduced  $\chi^2$  for CsErSe<sub>2</sub> is slightly lower for Model 1 ( $\chi_{redM1}^2 = 8.7$  vs  $\chi_{redM2}^2 = 10.4$ ). Assuming that similar chemical structures will lead to similar CEF Hamiltonians, only one model is correct. To adjudicate, we turn to bulk property measurements.

We computed the powder-averaged single-ion susceptibility from the CEF Hamiltonians for KErSe<sub>2</sub> [Fig. 4(a)-(b)] and CsErSe<sub>2</sub> [Fig. 4(e)-(f)] using PyCrystalField and compare to experimental data. Curiously, the powder-averaged susceptibilities for Models 1 and 2 are nearly identical for both compounds: the  $\chi^2$  differ by less than 0.2%. (For KErSe<sub>2</sub> inverse susceptibility  $10\text{ K} < T < 300\text{ K}$ ,  $\chi_{Model1}^2 = 349.6$  and  $\chi_{Model2}^2 = 349.4$ ; for CsErSe<sub>2</sub>,  $\chi_{Model1}^2 = 54.5$  and  $\chi_{Model2}^2 = 54.4$ .) Thus it is not possible to distinguish between the two models with powder susceptibility.

---

The lowest energy doublet for KErSe<sub>2</sub> is

$$|\psi_{\pm}\rangle = \pm 0.52(2) \left| \mp \frac{13}{2} \right\rangle - 0.508(5) \left| \mp \frac{7}{2} \right\rangle \pm 0.58(3) \left| \mp \frac{1}{2} \right\rangle + 0.347(6) \left| \pm \frac{5}{2} \right\rangle \pm 0.118(6) \left| \pm \frac{11}{2} \right\rangle, \quad (2)$$

and the lowest energy doublet for CsErSe<sub>2</sub> is

$$|\psi_{\pm}\rangle = \mp 0.59(4) \left| \mp \frac{13}{2} \right\rangle + 0.513(3) \left| \mp \frac{7}{2} \right\rangle \mp 0.51(5) \left| \mp \frac{1}{2} \right\rangle - 0.338(2) \left| \pm \frac{5}{2} \right\rangle \mp 0.123(9) \left| \pm \frac{11}{2} \right\rangle. \quad (3)$$

The full lists of eigenvalues and eigenstates are given in Tables VI and VII. The  $g$  tensors calculated from the ground state kets are  $g_{\perp} = 6.0(1)$  and  $g_z = 4.9(2)$  for KErSe<sub>2</sub>; and  $g_{\perp} = 5.4(3)$  and  $g_z = 5.9(5)$  for CsErSe<sub>2</sub>. For KErSe<sub>2</sub> the  $g$  tensor is easy-plane, but for CsErSe<sub>2</sub> both easy-axis and easy-plane  $g$ -tensors are within un-

Fortunately, Models 1 and 2 can be distinguished with directional magnetization. We computed the directional magnetization from the CEF Hamiltonians for KErSe<sub>2</sub> [Fig. 4(c)-(d)] and CsErSe<sub>2</sub> [Fig. 4(g)-(h)] using PyCrystalField and compare to experimental data. In this case, the bulk magnetization very clearly indicates which model is correct. Model 1 magnetization reveals an easy-plane ground state, while Model 2 magnetization reveals an easy-axis. As previously noted, experimental magnetization clearly shows both KErSe<sub>2</sub> and CsErSe<sub>2</sub> to have an easy-plane orthogonal to the  $c$  direction. Therefore, we identify Model 1 as the correct CEF model for both KErSe<sub>2</sub> and CsErSe<sub>2</sub>.

The correspondence between experimental and theoretical magnetization curves is not perfect because magnetic exchange interactions severely affect the shape of magnetization curves at low temperatures. This is particularly true for anisotropic exchange (which we expect for Er<sup>3+</sup>), where  $c$ -axis and  $ab$ -plane magnetization are

Table I. Best fit (Model 1) CEF parameters for KErSe<sub>2</sub> and CsErSe<sub>2</sub>. Four significant figures are given for each value regardless of uncertainty so that the CEF levels can be reproduced.

$B_n^m$ (meV)	KErSe <sub>2</sub>	CsErSe <sub>2</sub>
$B_2^0$	$(-2.773 \pm 0.33) \times 10^{-2}$	$(-3.559 \pm 0.64) \times 10^{-2}$
$B_4^0$	$(-3.987 \pm 0.05) \times 10^{-4}$	$(-3.849 \pm 0.11) \times 10^{-4}$
$B_4^3$	$(-1.416 \pm 0.02) \times 10^{-2}$	$(-1.393 \pm 0.03) \times 10^{-2}$
$B_6^0$	$(3.152 \pm 0.02) \times 10^{-6}$	$(3.154 \pm 0.04) \times 10^{-6}$
$B_6^3$	$(-7.616 \pm 1.94) \times 10^{-6}$	$(-4.695 \pm 3.56) \times 10^{-6}$
$B_6^6$	$(3.275 \pm 0.19) \times 10^{-5}$	$(3.381 \pm 0.37) \times 10^{-5}$

renormalized differently. Thus, we cannot expect quantitative agreement between low-T magnetization and experiment. Nevertheless, the overall anisotropy is clear.

The best fit CEF parameters, taken from Model 1, are given in Table I.

---

certainty. Both are in qualitative agreement with the anisotropy indicated by low-field magnetization. The uncertainties for these values were calculated by finding a line through parameter space which minimizes reduced  $\chi^2$  up to one standard deviation from the global minimum. This method, explained in detail in Appendix D,

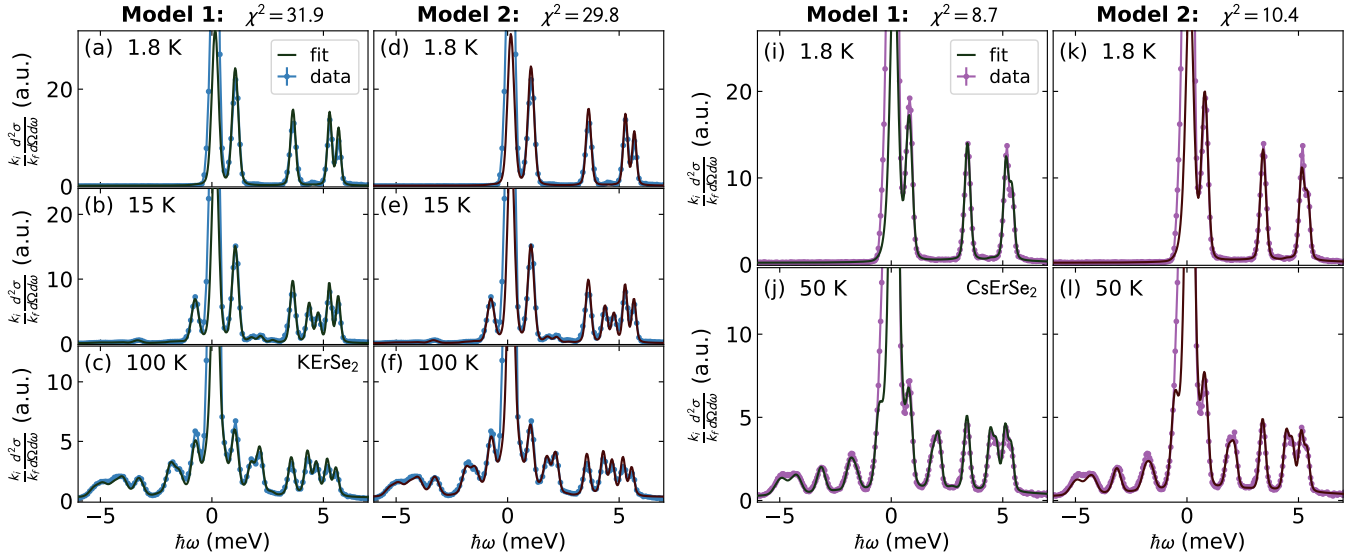


Figure 3. Crystal field fits to neutron scattering data for  $\text{KErSe}_2$  (a) - (f) and  $\text{CsErSe}_2$  and (i) - (l). Each column shows the fit for a different model, both of which fit the data well.

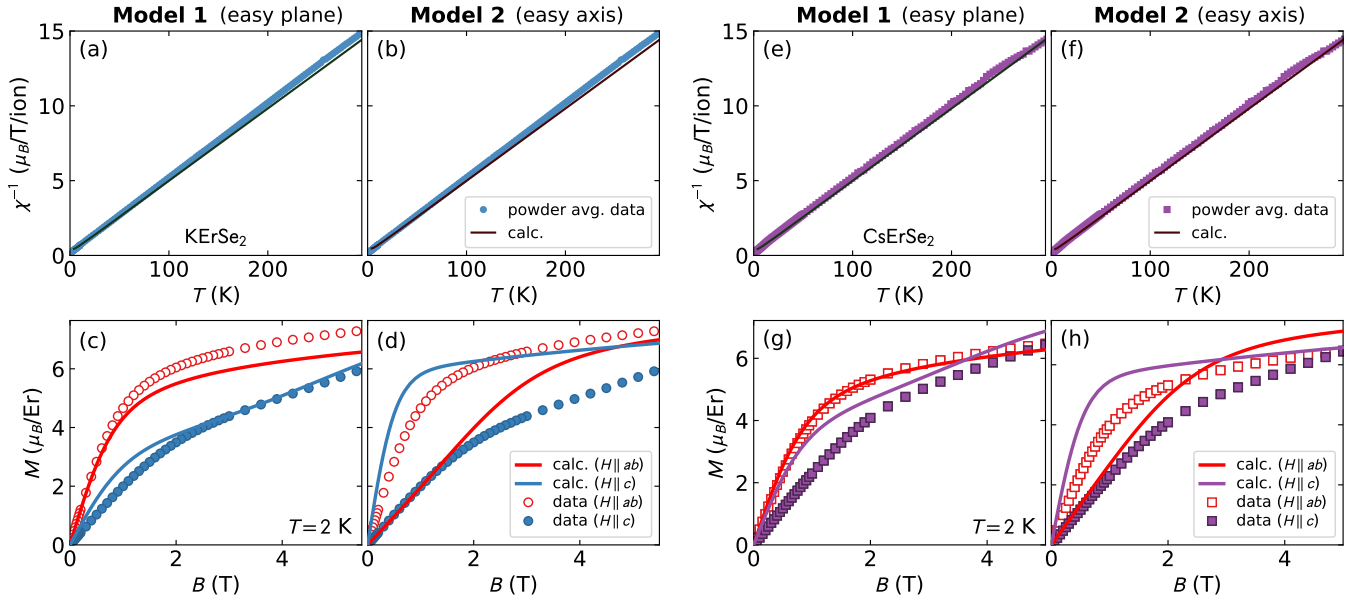


Figure 4. Calculated powder-average susceptibility and oriented magnetization for  $\text{KErSe}_2$  (a) - (d) and  $\text{CsErSe}_2$  and (e) - (h). For both compounds, the calculated powder-average susceptibility from Model 1 and Model 2 are indistinguishable. However, the low-temperature magnetization is very different: Model 1 predicts an easy-plane anisotropy, while Model 2 predicts an easy-axis. In both cases, Model 1 provides a better match for the data.

fully accounts for correlated uncertainties and gives accurate bounds on the final eigenstate coefficients.

#### IV. DISCUSSION

Both  $\text{KErSe}_2$  and  $\text{CsErSe}_2$  have an easy-plane magnetic anisotropy coinciding with the triangular lattice plane, just like their  $\text{Yb}^{3+}$  cousins [38, 39]. For both compounds, the ground state doublet has substantial weight

given to  $|\pm \frac{1}{2}\rangle$ ,  $|\pm \frac{7}{2}\rangle$ , and  $|\pm \frac{13}{2}\rangle$ . The similarity between the CEF ground states of these compounds shows that the difference between  $R\bar{3}m$  and  $P6_3/mmc$  does not produce a significant difference in anisotropy. Despite the different inter-layer arrangement of K and Cs ions, and the fact that the Se-octahedra of  $\text{KErSe}_2$  are  $0.032(5)$  Å taller along the  $c$  axis with an Er-Se distance  $0.008(7)$  Å shorter, the components of the ground state eigenstates almost overlap to within uncertainty.

The large  $|\pm \frac{1}{2}\rangle$  component in the CEF ground state

means that  $J_+$  and  $J_-$  will have a significant effect in causing tunnelling between these two states, but the  $|\pm \frac{7}{2}\rangle$  and  $|\pm \frac{13}{2}\rangle$  could suggest more classical behavior. Thus, an exotic finite-temperature quantum state like a QSL is a real possibility but not guaranteed.

Easy-plane  $\text{Er}^{3+}$  magnetism seems to be a robust feature of the delafossites: the  $\text{KErSe}_2$  and  $\text{CsErSe}_2$  CEF Hamiltonians are very similar to the CEF ground state reported for triangular-lattice  $\text{NaErS}_2$ , which also has easy-plane  $\text{Er}^{3+}$  ground state with substantial weight on  $|\pm \frac{1}{2}\rangle$  [28]. This is also similar to  $\text{Er}^{3+}$  pyrochlores  $\text{Er}_2\text{B}_2\text{O}_7$  ( $B = \text{Ge}, \text{Ti}, \text{Pt}, \text{and Sn}$ ) which likewise have easy-plane magnetic anisotropies from a  $D_3$  CEF environment [40]. In the pyrochlore  $\text{Er}_2\text{Ti}_2\text{O}_7$ , this easy-plane anisotropy leads to a degenerate ground state with emergent "clock anisotropies" in its magnetic ground state [41–43]. Given the similar  $XY$  CEF Hamiltonians, similar such behaviors could be found in the 2D triangular lattice  $\text{Er}^{3+}$  delafossites. Quantum order by disorder, which is theorized to govern  $\text{Er}_2\text{Ti}_2\text{O}_7$  [41], is also expected for triangular lattices [44], raising the possibility of emergent degeneracies on a 2D triangular lattice.

It is also worth noting that excited CEF states of  $\text{KErSe}_2$  and  $\text{CsErSe}_2$  are at very low energy, so we expect them to influence magnetic exchange interactions via virtual crystal field fluctuations [45, 46]. Accordingly, the crystal field eigenstates presented here will be relevant to future theoretical investigations of these compounds. To obtain more information on magnetic exchange, it will be necessary to measure at lower temperatures to ascertain whether these materials order magnetically and if so what type.

#### *Underconstrained CEF models*

On a different note, this analysis demonstrates that CEF fits to neutron data can be underconstrained. Model 1 and Model 2 fit the data almost equally well for both compounds, but have wildly different magnetic anisotropies. By  $\chi^2$  comparison alone, it is not possible to distinguish them—in fact for  $\text{KErSe}_2$  one would be tempted to incorrectly designate Model 2 as the correct model because its  $\chi_{red}^2$  is more than  $2\sigma$  below  $\chi_{red}^2$  of Model 1. Even comparison to powder-average susceptibility—commonly taken as a validation of a CEF Hamiltonian [47–50]—is insufficient to constrain the fit. One must compare the CEF transitions to single-crystal bulk-property experiments to fully constrain the solution. In this case, we use magnetization, which very clearly indicates the easy plane solution is correct.

It also is possible to identify the correct model by analyzing the CEF levels in a magnetic field. This splits the doublets, and creates more levels by which one can compare theory to experiment. This is done for  $\text{CsErSe}_2$  in Appendix C, and shows Model 1 to be closer to the observed scattering pattern, verifying the directional magnetization result. This method, however, is less useful

for powders because strong magnetic fields will cause the powder grains to reorient so that one is not measuring an isotropic powder-average, making the comparison between theory and experiment more qualitative than quantitative. Nevertheless, it is able to distinguish Model 1 and Model 2.

Because of the ambiguity revealed by this CEF analysis, we urge caution in interpreting CEF Hamiltonians extracted from neutron data. A solution may match the inelastic neutron data beautifully, but be totally inaccurate. Unfortunately, the practice of comparing CEF calculations to bulk single-crystal data is not common, so it is not possible to say how pervasive this underdetermination problem is. However the example of  $\text{Yb}_2\text{Ge}_2\text{O}_7$ , where the inelastic-neutron-scattering-fitted CEF Hamiltonian [51] failed to match the measured  $g$ -tensor from ESR [52], shows that the problem extends beyond the delafossites. At least for the  $D_3$  symmetric environment, single crystal bulk data or in-field scattering is necessary to fully constrain the solution.

## V. CONCLUSION

We have used crystal field excitations and bulk magnetization to determine the crystal field ground state and anisotropy of  $\text{KErSe}_2$  and  $\text{CsErSe}_2$ , both of which have easy-plane ground state doublets despite the different crystal space groups. We report the full CEF Hamiltonian, which has significant  $J_z = \frac{1}{2}$  components in the ground state doublet.

We also demonstrate that fitting the crystal field Hamiltonian to zero-field neutron scattering data can be an underdetermined problem, and requires single-crystal bulk property data to constrain the fit. This serves as a cautionary tale in interpreting CEF fits to neutron data.

These results suggest that quantum effects are significant in the Er-based delafossites at low temperatures, making them candidates for quantum effects or emergent degeneracies like  $\text{Er}_2\text{Ti}_2\text{O}_7$ . Additional low-temperature data is necessary to determine what, if any, is the ground state magnetic order. The lack of magnetic order and potential for strong quantum effects makes  $\text{KErSe}_2$  and  $\text{CsErSe}_2$  candidates for exotic magnetic states.

#### Acknowledgments

The research is supported by the U.S. Department of Energy (DOE), Office of Science, Basic Energy Sciences (BES), Materials Science and Engineering Division. This research at the Spallation Neutron Source was supported by the DOE Office of Science User Facilities Division. We also acknowledge helpful suggestions from Steve Nagler on fitting and statistics.

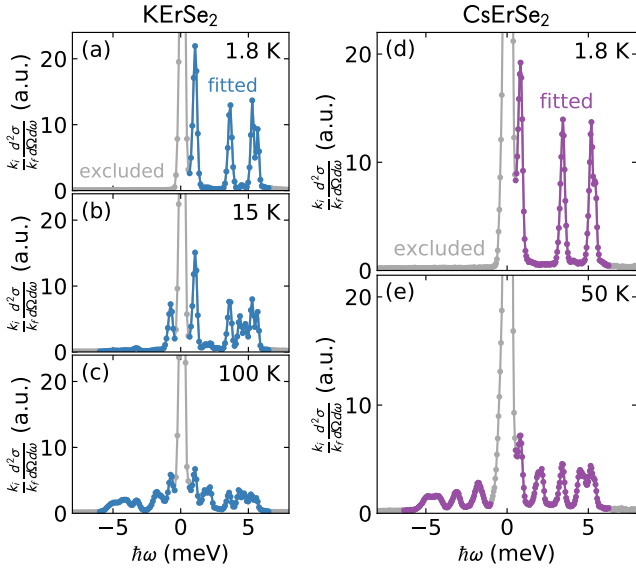


Figure 5. Data used to fit KErSe<sub>2</sub> (a)-(c) and CsErSe<sub>2</sub> (d)-(e). Fitted data points are in color, excluded data points are in grey.

### Appendix A: Fitted Data

We created 2D data sets to simplify the fitting procedure by integrating over  $1.25 \text{ \AA}^{-1} < Q < 1.9 \text{ \AA}^{-1}$ . We further simplified the data by excluding certain regions from the fitted data as shown in Fig. 5. The central elastic peak was excluded, as was the highest and lowest energy transfer data, which are featureless. We also excluded the negative energy transfer data for 1.8 K data because the Boltzmann population factor suppresses the negative energy peaks and there is no information there. At higher temperatures the negative energy peaks are visible, so we kept these in the range of fitted data.

We also collected neutron scattering data at  $E_i = 30 \text{ meV}$  for CsErSe<sub>2</sub>, shown in Fig. 6. No peaks were visible in the data, and because of this the data was not used in the fits. Both Model 1 and Model 2 predict three CEF transitions around 25 meV, but for neither model do the peaks have any appreciable intensity. Model 1 calculated intensity is shown in Fig. 6, and no calculated peaks are visible, consistent with the data.

### Appendix B: Fitting procedure

#### 1. Fitted variables

In addition to the six CEF parameters, we included several fitted parameters in order to properly model the neutron spectrum. We fitted an overall intensity factor (different for each compound). We also included a linear fitted background in KErSe<sub>2</sub>. The background in CsErSe<sub>2</sub> was larger and more complex because of the

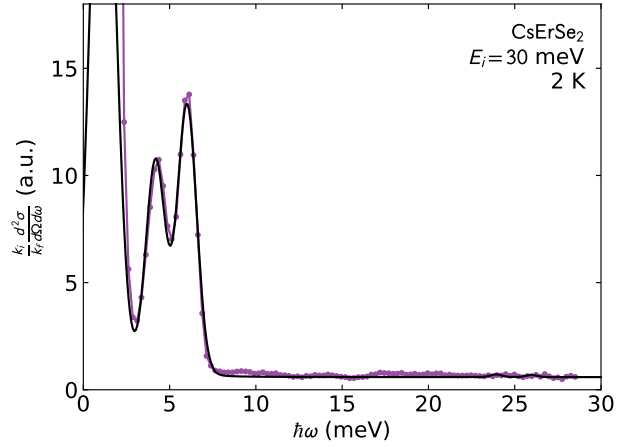


Figure 6. Observed and calculated scattering for CsErSe<sub>2</sub> with  $E_i = 30 \text{ meV}$ . Three doublets exist at 23.0 meV, 24.9 meV, and 25.2 meV in Model 1, but the calculated scattering is too weak to be observed. This is consistent with the data.

magnet used in the experiment, so we modeled the background with two broad Gaussians, adjusted by hand so that the background in between the CEF peaks matched experiment.

To model the peak shape, we used a Voigt profile to simulate a convoluted Gaussian and Lorentzian. The Gaussian component was defined by a phenomenological resolution function which models resolution width as a linear function of energy. The slope and offset of this line were fitted to the widths of fitted 1.8 K peak widths (excluding the central elastic peak). Each compound had its own resolution function, and it was fixed for the entire fitting procedure. The Lorentzian component was treated as a fitted variable, constant as a function of energy but variable with temperature. We also fitted a global offset in energy for each compound to account for slight asymmetries in the resolution function. As shown by the fits in Fig. 3, this phenomenological peak shape fits the data very well.

In the final stages of the fit, it became clear that the peaks in the higher  $T$  data slightly shifted to lower energies (and the negative energy transfer peaks were shifted to higher energies). This is due to thermal expansion shifting the ligands very slightly away from the central Er<sup>3+</sup> ion, which lowers the overall energy scale of the CEF interactions. To account for this, we added a fitted thermal expansion parameter which multiplies the CEF transition energy by a factor varying linearly with temperature, so that

$$\Delta = \Delta_{calc}(1 - ET)$$

where  $\Delta$  is the peak energy,  $E$  is the thermal expansion parameter, and  $T$  is temperature.

In total, this gives 15 fitted parameters for KErSe<sub>2</sub> and 11 fitted parameters for CsErSe<sub>2</sub>. The peak width, background, energy offset, and thermal expansion parameters were only fitted in the final stages—once the peak

energies and intensities had converged roughly to their experimental values.

## 2. Fitting protocol

Following the method in ref. [53], we first fitted a point charge model and then directly fitted the CEF parameters. We fitted the point charge model by varying the size of the Se octahedra and the compression along the  $c$  axis (the only ways to modify the ligand environment while preserving all symmetries). Then, using the calculated CEF parameters from the fitted point charge model as starting parameters, we fit the CEF parameters directly to the data iteratively using SciPy's implementation of the Powell [54] and Nelder-Mead [55] methods. We fit using one method, then multiplied the scale factor by a factor to "kick it" out of the local minimum, refit using the other method, etc. This was repeated until iterations failed to reduce the global  $\chi^2$  value.

For the first few iterations, we added a term to the global  $\chi^2$

$$\chi_{energy}^2 = \sum_i (\Delta_{calc_i} - \Delta_{exp_i})^2 \quad (\text{B1})$$

based off the fitted transition energies  $\Delta_{exp_i}$  for the lowest temperature data set. This was to smooth out the  $\chi^2$  landscape and ensure the peaks converged to the right energies. Once the fitted peaks were close to the observed peak energies, we removed this term.

This procedure yielded good convergence to the global minimum: both KErSe<sub>2</sub> and CsErSe<sub>2</sub> converged to the lowest global  $\chi^2$  (even though for KErSe<sub>2</sub> the model with lowest  $\chi^2$  turned out to be incorrect). The code for these fits, which gives the precise protocols and all intermediate fitted values, can be found at <https://github.com/aschel/PyCrystalField>.

## 3. Fit results

The fitted CEF parameters for Model 1 and Model 2 for KErSe<sub>2</sub> are listed in Table II and for CsErSe<sub>2</sub> are listed in Table III. Single-crystal bulk property measurements were able to identify Model 1 as the correct model for both compounds.

### Appendix C: Finite-field scattering

The CsErSe<sub>2</sub> experiment was performed with a vertical field magnet, and we collected data at 3 T, 5 T, 1 T and 2 T (in that order) in addition to 0 T. This data is shown in Fig. 7, and shows the doublets being split by the magnetic field. Applying the magnetic field dramatically attenuated the neutron signal from the material (but not the background), indicating that the loose powder grains

Table II. Fitted CEF parameters for KErSe<sub>2</sub>

$B_n^m$ (meV)	Model 1	Model 2
$B_2^0$	$-2.773 \times 10^{-2}$	$2.720 \times 10^{-2}$
$B_4^0$	$-3.987 \times 10^{-4}$	$-4.864 \times 10^{-4}$
$B_4^3$	$-1.416 \times 10^{-2}$	$1.282 \times 10^{-2}$
$B_6^0$	$3.152 \times 10^{-6}$	$1.028 \times 10^{-6}$
$B_6^3$	$-7.616 \times 10^{-6}$	$4.764 \times 10^{-5}$
$B_6^6$	$3.275 \times 10^{-5}$	$2.113 \times 10^{-5}$

Table III. Fitted CEF parameters for CsErSe<sub>2</sub>

$B_n^m$ (meV)	Model 1	Model 2
$B_2^0$	$-3.559 \times 10^{-2}$	$3.114 \times 10^{-2}$
$B_4^0$	$-3.849 \times 10^{-4}$	$-4.718 \times 10^{-4}$
$B_4^3$	$-1.393 \times 10^{-2}$	$1.259 \times 10^{-2}$
$B_6^0$	$3.154 \times 10^{-6}$	$9.324 \times 10^{-7}$
$B_6^3$	$-4.695 \times 10^{-6}$	$4.715 \times 10^{-5}$
$B_6^6$	$3.381 \times 10^{-5}$	$2.011 \times 10^{-5}$

were shifted out of the beam (though still in the sample can) by the magnetic field. This shifting almost certainly involved a reorientation in the powder grains—meaning that the magnetic field was preferentially applied along certain crystallographic directions.

The shifts and reorientation notwithstanding, we simulated the powder-average in-field neutron spectrum using PyCrystalField with field directions randomly sampled around a unit sphere. These simulations are plotted in Fig. 7 for Model 1 (green) and Model 2 (red). The match between theory and experiment is not perfect, indicating the effects of grain reorientation, small magnetoelastic effects, or an slightly inaccurate Hamiltonian. Nevertheless, on a qualitative level, Model 1 matches the data much better than Model 2—particularly in the splitting of the low-energy mode at 3 T and 5 T.

### Appendix D: Uncertainty

The uncertainties of CEF parameters are strongly correlated due to the nonlinear dependence of the peak energies on the CEF parameters. To characterize this uncertainty, we found the maximum deviation of all variables from the best fit values which would increase global reduced  $\chi^2$  by one standard deviation. We began by defining a range of  $B_2^0$  values around the best fit  $B_2^0$  value, and for each  $B_2^0$  we re-fit the neutron data keeping  $B_2^0$  fixed and varying all other variables. This resulted in a line through parameter space as a function of  $B_2^0$ , giving a range of solutions which fit the data approximately equally. These solutions, with the associated  $\chi^2$  and comparison to magnetization, are plotted in Fig. 8 (KErSe<sub>2</sub>) and Fig. 9 (CsErSe<sub>2</sub>).

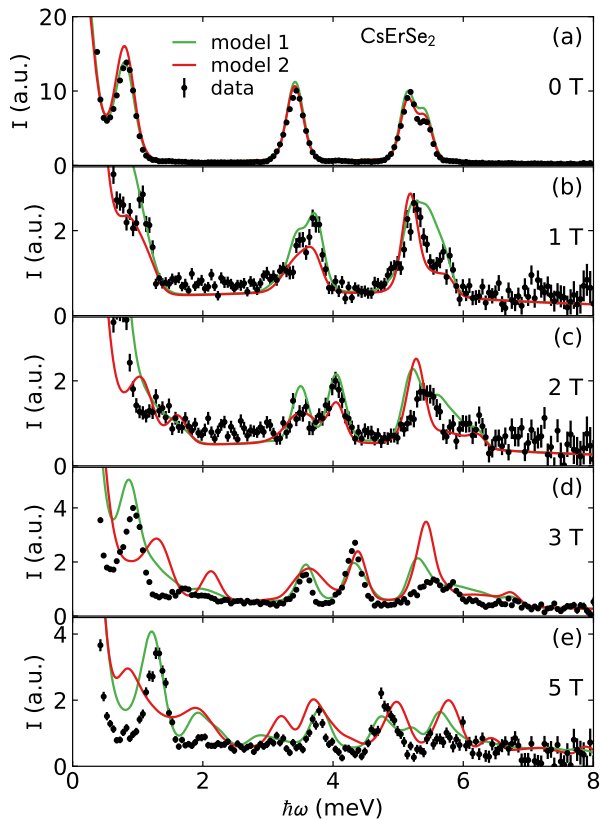


Figure 7. Nonzero-field CEF scattering for CsErSe<sub>2</sub>. Simulated scattering from Model 1 and Model 2 assuming a powder average are plotted in green and red, respectively. Neither model is perfect due to the imperfect powder average, but Model 1 is qualitatively closer to the measured scattering.

We then truncated the range of  $B_2^0$  to where global  $\chi_{red}^2$  increased above the best fit value by one (indicating one standard deviation because reduced  $\chi^2$  is normalized to the one-standard-deviation uncertainty and the number of free parameters). This yielded an approximately linear relationship between  $B_2^0$  and all the other fitted variables for this range, which we fit to a quadratic curve (the parameters for these curves are given in Tables IV and V). As shown in Figs. 8 and 9, the differences in the neutron spectrum along the best fit line are barely noticeable. Differences in  $c$ -axis single-ion low-field magnetization are visible, but due to the strong non-trivial effects of magnetic exchange on low-temperature magnetization, we did not include magnetization in the global  $\chi^2$  calculations.

This gave us the uncertainty in the CEF parameters  $B_n^m$  reported in Table I. However, because the relation-

ship between CEF parameters and CEF transition intensities is complex and nonlinear, these uncertainties do not straightforwardly propagate into uncertainties of the eigenstates. To find the eigenstate uncertainties, we diagonalized a series of CEF Hamiltonian from the range of solutions given by the best fit lines in Tables IV and V. We found the shifts in eigenvector component contri-

Table IV. Best fit curve through parameter space for KErSe<sub>2</sub>, where variable =  $a + b(B_2^0) + c(B_2^0)^2$ . LW refers to the Lorentzian width of the peaks.

Variable	a	b	c
scale factor	0.000513(6)	-0.0014(2)	-0.018(3)
$B_4^0$	-0.0004389(7)	-0.00127(5)	0.0064(3)
$B_4^3$	-0.01241(5)	0.0732(1)	0.36(2)
$B_6^0$	$2.995(9) \times 10^{-6}$	$-5.8(7) \times 10^{-6}$	$-6(6) \times 10^{-6}$
$B_6^3$	$-2.669(8) \times 10^{-5}$	-0.000809(6)	-0.00435(5)
$B_6^6$	$1.6(7) \times 10^{-5}$	-0.00063(5)	-0.001(2)
$LW_{1.8\text{ K}}$	0.059(4)	-0.1(3)	0.2(5)
$LW_{15\text{ K}}$	0.069(7)	0.3(6)	10(10)
$LW_{100\text{ K}}$	0.147(9)	1.1(7)	20(10)
$\hbar\omega$ offset	0.152(2)	0.2(1)	-2.7(3)
therm. expan.	0.00019(5)	0.0(3)	0.04(5)

Table V. Best fit curve through parameter space for CsErSe<sub>2</sub>, where variable =  $a + b(B_2^0) + c(B_2^0)^2$ . LW refers to the Lorentzian width of the peaks.

Variable	a	b	c
scale factor	0.43(3)	0.3(1)	8.4(8)
$B_4^0$	-0.000433(7)	-0.00099(5)	0.0101(3)
$B_4^3$	-0.01117(5)	0.1123(8)	0.97(1)
$B_6^0$	$2.946(9) \times 10^{-6}$	$-5.2(7) \times 10^{-6}$	$1.7(6) \times 10^{-5}$
$B_6^3$	$-2.765(8) \times 10^{-5}$	-0.000749(6)	-0.00292(5)
$B_6^6$	$8.48(8) \times 10^{-6}$	-0.000869(6)	-0.00442(5)
$LW_{1.8\text{ K}}$	0.073(3)	0.9(1)	15.7(6)
$LW_{50\text{ K}}$	0.077(7)	0.7(3)	16.6(3)
$\hbar\omega$ offset	0.15(2)	0.63(8)	0.1(0)
therm. expan.	$-7(5) \times 10^{-5}$	-0.007(5)	-0.04(6)

Contributions to be approximately symmetric about the best fit values in the range bounded by one  $\chi^2$  standard deviation, so we defined uncertainty to be the difference between the best fit value and the value at the extremes of the best fit line. These uncertainties are reported for the ground state in Eqs. 2-3, and the full list of eigenstates with associated uncertainties is given in Table VI (KErSe<sub>2</sub>) and Table VII (CsErSe<sub>2</sub>).

[1] J. Knolle and R. Moessner, *Annual Review of Condensed Matter Physics* **10**, 451 (2019).

[2] L. Balents, *Nature* **464**, 199 (2010).

[3] L. Savary and L. Balents, *Reports on Progress in Physics*

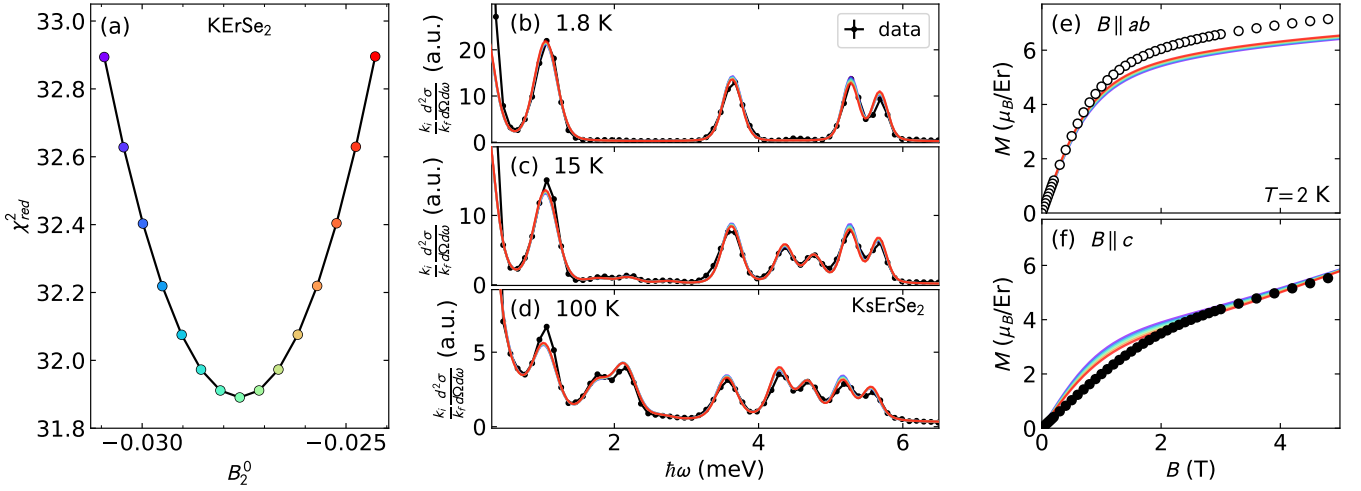


Figure 8. Uncertainty in fitted KErSe<sub>2</sub> CEF parameters for Model 1. (a)  $\chi_{red}^2$  as a function of  $B_2^0$ , allowing all other parameters to vary, up to one standard deviation. (b)-(d) Calculated neutron spectrum for the range of  $B_2^0$ , with  $B_2^0$  value indicated by the colors in panel (a). The various curves are nearly indistinguishable. (e)-(f) Magnetization for the range of  $B_2^0$ .

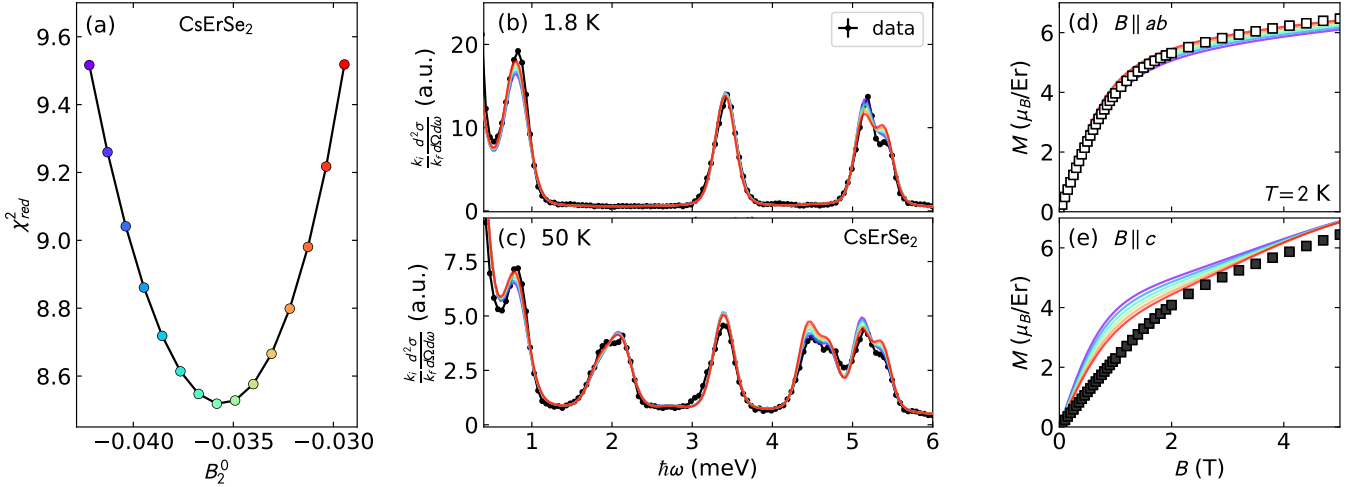


Figure 9. Uncertainty in fitted CsErSe<sub>2</sub> CEF parameters for Model 1. (a)  $\chi_{red}^2$  as a function of  $B_2^0$ , allowing all other parameters to vary, up to one standard deviation. (b)-(c) Calculated neutron spectrum for the range of  $B_2^0$ , with  $B_2^0$  value indicated by the colors in panel (a). The various curves are nearly indistinguishable. (d)-(e) Magnetization for the range of  $B_2^0$ .

- 80**, 016502 (2016).
- [4] L. Capriotti, A. E. Trumper, and S. Sorella, *Phys. Rev. Lett.* **82**, 3899 (1999).
- [5] D. A. Huse and V. Elser, *Phys. Rev. Lett.* **60**, 2531 (1988).
- [6] Z. Zhu and S. R. White, *Phys. Rev. B* **92**, 041105(R) (2015).
- [7] Z. Zhu, P. A. Maksimov, S. R. White, and A. L. Chernyshev, *Phys. Rev. Lett.* **120**, 207203 (2018).
- [8] Y. Zhou, K. Kanoda, and T.-K. Ng, *Rev. Mod. Phys.* **89**, 025003 (2017).
- [9] P. A. Maksimov, Z. Zhu, S. R. White, and A. L. Chernyshev, *Phys. Rev. X* **9**, 021017 (2019).
- [10] W. Witczak-Krempa, G. Chen, Y. B. Kim, and L. Balents, *Annual Review of Condensed Matter Physics* **5**, 57 (2014).
- [11] Y.-D. Li, X. Wang, and G. Chen, *Phys. Rev. B* **94**, 035107 (2016).
- [12] J. Iaconis, C. Liu, G. B. Halász, and L. Balents, *SciPost Phys.* **4**, 003 (2018).
- [13] Y. Li, G. Chen, W. Tong, L. Pi, J. Liu, Z. Yang, X. Wang, and Q. Zhang, *Phys. Rev. Lett.* **115**, 167203 (2015).
- [14] Y. Li, D. Adroja, P. K. Biswas, P. J. Baker, Q. Zhang, J. Liu, A. A. Tsirlin, P. Gegenwart, and Q. Zhang, *Phys. Rev. Lett.* **117**, 097201 (2016).
- [15] Y. Shen, Y.-D. Li, H. Wo, Y. Li, S. Shen, B. Pan, Q. Wang, H. C. Walker, P. Steffens, M. Boehm, Y. Hao, D. L. Quintero-Castro, L. W. Harriger, M. D. Frontzek, L. Hao, S. Meng, Q. Zhang, G. Chen, and J. Zhao, *Nature* **540**, 559 (2016).
- [16] J. A. M. Paddison, M. Daum, Z. Dun, G. Ehlers, Y. Liu, M. Stone, H. Zhou, and M. Mourigal, *Nature Physics* **13**, 117 (2017).
- [17] Y. Xu, J. Zhang, Y. S. Li, Y. J. Yu, X. C. Hong, Q. M.

Table VI. Eigenvectors and Eigenvalues for KErSe<sub>2</sub>

Eigenvalues (meV)	Eigenvectors					
0.0		0.52(2)   - $\frac{13}{2}$	-0.508(5)   - $\frac{7}{2}$	+0.58(3)   - $\frac{1}{2}$	+0.347(6)   $\frac{5}{2}$	+0.118(6)   $\frac{11}{2}$
0.0		-0.118(6)   - $\frac{11}{2}$	+0.347(6)   - $\frac{5}{2}$	-0.58(3)   $\frac{1}{2}$	-0.508(5)   $\frac{7}{2}$	-0.52(2)   $\frac{13}{2}$
0.903(1)	0.718(9)   - $\frac{15}{2}$	-0.484(3)   - $\frac{9}{2}$	+0.41(2)   - $\frac{3}{2}$	+0.28(6)   $\frac{3}{2}$	+0.07(7)   $\frac{9}{2}$	+0.1(1)   $\frac{15}{2}$
0.903(1)	-0.1(1)   - $\frac{15}{2}$	+0.07(7)   - $\frac{9}{2}$	-0.28(6)   - $\frac{3}{2}$	+0.41(2)   $\frac{3}{2}$	+0.484(3)   $\frac{9}{2}$	+0.718(9)   $\frac{15}{2}$
3.491(3)		-0.7(4)   - $\frac{13}{2}$	+0.1(2)   - $\frac{7}{2}$	+0.7(4)   - $\frac{1}{2}$	+0.1(2)   $\frac{5}{2}$	-0.1(2)   $\frac{11}{2}$
3.491(3)		-0.083(4)   - $\frac{11}{2}$	-0.1(2)   - $\frac{5}{2}$	+0.68(1)   $\frac{1}{2}$	-0.11(3)   $\frac{7}{2}$	-0.71(9)   $\frac{13}{2}$
5.134(3)		-0.708(7)   - $\frac{11}{2}$	+0.62(1)   - $\frac{5}{2}$	+0.244(9)   $\frac{1}{2}$	+0.0828(9)   $\frac{7}{2}$	+0.2202(1)   $\frac{13}{2}$
5.134(3)		-0.2202(1)   - $\frac{13}{2}$	+0.0828(9)   - $\frac{7}{2}$	-0.244(9)   - $\frac{1}{2}$	+0.62(1)   $\frac{5}{2}$	+0.708(7)   $\frac{11}{2}$
5.538(1)	-0.0(6)   - $\frac{15}{2}$	+0.05(3)   - $\frac{9}{2}$	-0.34(7)   - $\frac{3}{2}$	+0.66(4)   $\frac{3}{2}$	+0.2(1)   $\frac{9}{2}$	-0.64(1)   $\frac{15}{2}$
5.538(1)	-0.64(1)   - $\frac{15}{2}$	-0.2(1)   - $\frac{9}{2}$	+0.66(4)   - $\frac{3}{2}$	+0.34(7)   $\frac{3}{2}$	+0.05(3)   $\frac{9}{2}$	+0.0(6)   $\frac{15}{2}$
23.3(3)		0.607(1)   - $\frac{11}{2}$	+0.529(5)   - $\frac{5}{2}$	+0.34(2)   $\frac{1}{2}$	-0.421(7)   $\frac{7}{2}$	+0.2471(7)   $\frac{13}{2}$
23.3(3)		0.2471(7)   - $\frac{13}{2}$	+0.421(7)   - $\frac{7}{2}$	+0.34(2)   - $\frac{1}{2}$	-0.529(5)   $\frac{5}{2}$	+0.607(1)   $\frac{11}{2}$
25.2(3)	0.267(9)   - $\frac{15}{2}$	+0.848(4)   - $\frac{9}{2}$	+0.43(1)   - $\frac{3}{2}$	+0.156(8)   $\frac{3}{2}$	+0.021(3)   $\frac{9}{2}$	+0.0(7)   $\frac{15}{2}$
25.2(3)	0.0(8)   - $\frac{15}{2}$	-0.021(3)   - $\frac{9}{2}$	+0.156(8)   - $\frac{3}{2}$	-0.43(1)   $\frac{3}{2}$	+0.848(4)   $\frac{9}{2}$	-0.267(9)   $\frac{15}{2}$
25.4(3)		-0.3(3)   - $\frac{11}{2}$	-0.5(5)   - $\frac{5}{2}$	+0.1(1)   $\frac{1}{2}$	-0.7(7)   $\frac{7}{2}$	+0.3(3)   $\frac{13}{2}$
25.4(3)		-0.3(3)   - $\frac{13}{2}$	-0.7(7)   - $\frac{7}{2}$	-0.1(1)   - $\frac{1}{2}$	-0.5(5)   $\frac{5}{2}$	+0.3(3)   $\frac{11}{2}$

Table VII. Eigenvectors and Eigenvalues for CsErSe<sub>2</sub>

Eigenvalues (meV)	Eigenvectors					
0.0	0.123(9)   - $\frac{11}{2}$	-0.338(2)   - $\frac{5}{2}$	+0.51(5)   $\frac{1}{2}$	+0.513(3)   $\frac{7}{2}$	+0.59(4)   $\frac{13}{2}$	
0.0	-0.59(4)   - $\frac{13}{2}$	+0.513(3)   - $\frac{7}{2}$	-0.51(5)   - $\frac{1}{2}$	-0.338(2)   $\frac{5}{2}$	-0.123(9)   $\frac{11}{2}$	
0.675(5)	0.03(7)   - $\frac{9}{2}$	-0.2(4)   - $\frac{3}{2}$	+0.4(7)   $\frac{3}{2}$	+0.5(9)   $\frac{9}{2}$	+0.8(6)   $\frac{15}{2}$	
0.675(5)	-0.8(6)   - $\frac{15}{2}$	+0.5(9)   - $\frac{9}{2}$	-0.4(7)   - $\frac{3}{2}$	-0.2(4)   $\frac{3}{2}$	-0.03(7)   $\frac{9}{2}$	
3.29(7)	0.68(3)   - $\frac{13}{2}$	-0.04(5)   - $\frac{7}{2}$	-0.71(2)   - $\frac{1}{2}$	-0.17(4)   $\frac{5}{2}$	+0.04(1)   $\frac{11}{2}$	
3.29(7)	0.04(1)   - $\frac{11}{2}$	+0.17(4)   - $\frac{5}{2}$	-0.71(2)   $\frac{1}{2}$	+0.04(5)   $\frac{7}{2}$	+0.68(3)   $\frac{13}{2}$	
5.02(1)	0.1852(6)   - $\frac{13}{2}$	-0.074(3)   - $\frac{7}{2}$	+0.28(2)   - $\frac{1}{2}$	-0.59(2)   $\frac{5}{2}$	-0.73(1)   $\frac{11}{2}$	
5.02(1)	-0.73(1)   - $\frac{11}{2}$	+0.59(2)   - $\frac{5}{2}$	+0.28(2)   $\frac{1}{2}$	+0.074(3)   $\frac{7}{2}$	+0.1852(6)   $\frac{13}{2}$	
5.28(1)	0.06(5)   - $\frac{9}{2}$	-0.4(1)   - $\frac{3}{2}$	+0.67(7)   $\frac{3}{2}$	+0.26(3)   $\frac{9}{2}$	-0.58(2)   $\frac{15}{2}$	
5.28(1)	0.58(2)   - $\frac{15}{2}$	+0.26(3)   - $\frac{9}{2}$	-0.67(7)   - $\frac{3}{2}$	-0.4(1)   $\frac{3}{2}$	-0.06(5)   $\frac{9}{2}$	
23.1(5)	-0.239(2)   - $\frac{13}{2}$	-0.428(8)   - $\frac{7}{2}$	-0.36(3)   - $\frac{1}{2}$	+0.531(7)   $\frac{5}{2}$	-0.59(2)   $\frac{11}{2}$	
23.1(5)	0.59(2)   - $\frac{11}{2}$	+0.531(7)   - $\frac{5}{2}$	+0.36(3)   $\frac{1}{2}$	-0.428(8)   $\frac{7}{2}$	+0.239(2)   $\frac{13}{2}$	
24.9(5)	-0.25(2)   - $\frac{15}{2}$	-0.843(8)   - $\frac{9}{2}$	-0.45(2)   - $\frac{3}{2}$	-0.17(1)   $\frac{3}{2}$	-0.025(6)   $\frac{9}{2}$	
24.9(5)	0.025(6)   - $\frac{9}{2}$	-0.17(1)   - $\frac{3}{2}$	+0.45(2)   $\frac{3}{2}$	-0.843(8)   $\frac{9}{2}$	+0.25(2)   $\frac{15}{2}$	
25.2(6)	-0.32(2)   - $\frac{13}{2}$	-0.74(6)   - $\frac{7}{2}$	-0.136(1)   - $\frac{1}{2}$	-0.47(2)   $\frac{5}{2}$	+0.3262(5)   $\frac{11}{2}$	
25.2(6)	-0.3262(5)   - $\frac{11}{2}$	-0.47(2)   - $\frac{5}{2}$	+0.136(1)   $\frac{1}{2}$	-0.74(6)   $\frac{7}{2}$	+0.32(2)   $\frac{13}{2}$	

Zhang, and S. Y. Li, *Phys. Rev. Lett.* **117**, 267202 (2016).

- [18] Y. Li, D. Adroja, R. I. Bewley, D. Voneshen, A. A. Tsrilin, P. Gegenwart, and Q. Zhang, *Phys. Rev. Lett.* **118**, 107202 (2017).
- [19] Y.-D. Li, Y. Shen, Y. Li, J. Zhao, and G. Chen, *Phys. Rev. B* **97**, 125105 (2018).
- [20] Z. Zhu, P. A. Maksimov, S. R. White, and A. L. Chernyshev, *Phys. Rev. Lett.* **119**, 157201 (2017).
- [21] I. Kimchi, A. Nahum, and T. Senthil, *Phys. Rev. X* **8**, 031028 (2018).
- [22] Z. Ma, J. Wang, Z.-Y. Dong, J. Zhang, S. Li, S.-H. Zheng, Y. Yu, W. Wang, L. Che, K. Ran, S. Bao, Z. Cai, P. Čermák, A. Schneidewind, S. Yano, J. S. Gardner, X. Lu, S.-L. Yu, J.-M. Liu, S. Li, J.-X. Li, and J. Wen, *Phys. Rev. Lett.* **120**, 087201 (2018).
- [23] W. Liu, Z. Zhang, J. Ji, Y. Liu, J. Li, X. Wang, H. Lei, G. Chen, and Q. Zhang, *Chinese Physics Letters* **35**, 117501 (2018).
- [24] M. Baenitz, P. Schlender, J. Sichelschmidt, Y. A. Onykiienko, Z. Zangeneh, K. M. Ranjith, R. Sarkar, L. Hozoi, H. C. Walker, J.-C. Orain, H. Yasuoka, J. van den Brink, H. H. Klauss, D. S. Inosov, and T. Doert, *Phys. Rev. B* **98**, 220409(R) (2018).
- [25] M. M. Bordelon, E. Kenney, C. Liu, T. Hogan, L. Posthuma, M. Kavand, Y. Lyu, M. Sherwin, N. P.

- Butch, C. Brown, M. J. Graf, L. Balents, and S. D. Wilson, *Nature Physics* **15**, 1058 (2019).
- [26] K. M. Ranjith, D. Dmytriieva, S. Khim, J. Sichelschmidt, S. Luther, D. Ehlers, H. Yasuoka, J. Wosnitza, A. A. Tsirlin, H. Kühne, and M. Baenitz, *Phys. Rev. B* **99**, 180401(R) (2019).
- [27] R. Sarkar, P. Schlender, V. Grinenko, E. Haeussler, P. J. Baker, T. Doert, and H.-H. Klauss, *Phys. Rev. B* **100**, 241116(R) (2019).
- [28] S. Gao, F. Xiao, K. Kamazawa, K. Ikeuchi, D. Biner, K. Krämer, C. Rüegg, and T.-h. Arima, *arXiv preprint arXiv:1911.10662* (2019).
- [29] M. Ashtar, M. A. Marwat, Y. X. Gao, Z. T. Zhang, L. Pi, S. L. Yuan, and Z. M. Tian, *J. Mater. Chem. C* **7**, 10073 (2019).
- [30] M. Hutchings, *Solid State Physics*, **16**, 227 (1964).
- [31] S. Edvardsson and M. Klintonberg, *Journal of Alloys and Compounds* **275-277**, 230 (1998).
- [32] J. G. Rau and M. J. P. Gingras, *Phys. Rev. B* **92**, 144417 (2015).
- [33] A. Furrer, J. Mesot, and T. Strässle, *Neutron scattering in condensed matter physics* (World Scientific, 2009).
- [34] J. Xing, L. D. Sanjeewa, J. Kim, G. Stewart, M.-H. Du, F. A. Reboredo, R. Custelcean, and A. S. Sefat, *ACS Materials Letters* (2019), 10.1021/acsmaterialslett.9b00464.
- [35] J. Xing, L. D. Sanjeewa, J. Kim, W. R. Meier, A. F. May, Q. Zheng, R. Custelcean, G. R. Stewart, and A. S. Sefat, *Phys. Rev. Materials* **3**, 114413 (2019).
- [36] K. W. H. Stevens, *Proceedings of the Physical Society. Section A* **65**, 209 (1952).
- [37] A. Scheie, “Pycrystalfield,” <https://github.com/asche1/PyCrystalField> (2018).
- [38] Z. Zangeneh, S. Avdoshenko, J. van den Brink, and L. Hozoi, *Phys. Rev. B* **100**, 174436 (2019).
- [39] J. Sichelschmidt, P. Schlender, B. Schmidt, M. Baenitz, and T. Doert, *Journal of Physics: Condensed Matter* **31**, 205601 (2019).
- [40] J. Gaudet, A. M. Hallas, A. I. Kolesnikov, and B. D. Gaulin, *Phys. Rev. B* **97**, 024415 (2018).
- [41] K. A. Ross, Y. Qiu, J. R. D. Copley, H. A. Dabkowska, and B. D. Gaulin, *Phys. Rev. Lett.* **112**, 057201 (2014).
- [42] J. Gaudet, A. M. Hallas, J. Thibault, N. P. Butch, H. A. Dabkowska, and B. D. Gaulin, *Phys. Rev. B* **95**, 054407 (2017).
- [43] M. E. Zhitomirsky, P. C. W. Holdsworth, and R. Moessner, *Phys. Rev. B* **89**, 140403(R) (2014).
- [44] P. Lecheminant, B. Bernu, C. Lhuillier, and L. Pierre, *Phys. Rev. B* **52**, 6647 (1995).
- [45] S. Petit, J. Robert, S. Guitteny, P. Bonville, C. Decorse, J. Ollivier, H. Mutka, M. J. P. Gingras, and I. Mirebeau, *Phys. Rev. B* **90**, 060410(R) (2014).
- [46] J. G. Rau, S. Petit, and M. J. P. Gingras, *Phys. Rev. B* **93**, 184408 (2016).
- [47] A. J. Princep, D. Prabhakaran, A. T. Boothroyd, and D. T. Adroja, *Phys. Rev. B* **88**, 104421 (2013).
- [48] A. D. Christianson, J. M. Lawrence, P. G. Pagliuso, N. O. Moreno, J. L. Sarrao, J. D. Thompson, P. S. Riseborough, S. Kern, E. A. Goremychkin, and A. H. Lacerda, *Phys. Rev. B* **66**, 193102 (2002).
- [49] J. Gaudet, E. M. Smith, J. Dudemaine, J. Beare, C. R. C. Buhariwalla, N. P. Butch, M. B. Stone, A. I. Kolesnikov, G. Xu, D. R. Yahne, K. A. Ross, C. A. Marjerrison, J. D. Garrett, G. M. Luke, A. D. Bianchi, and B. D. Gaulin, *Phys. Rev. Lett.* **122**, 187201 (2019).
- [50] J. Xu, V. K. Anand, A. K. Bera, M. Frontzek, D. L. Abernathy, N. Casati, K. Siemensmeyer, and B. Lake, *Phys. Rev. B* **92**, 224430 (2015).
- [51] A. M. Hallas, J. Gaudet, M. N. Wilson, T. J. Munsie, A. A. Aczel, M. B. Stone, R. S. Freitas, A. M. Arevalo-Lopez, J. P. Attfield, M. Tachibana, C. R. Wiebe, G. M. Luke, and B. D. Gaulin, *Phys. Rev. B* **93**, 104405 (2016).
- [52] C. Sarkis, J. Rau, L. Sanjeewa, M. Powell, J. Kolis, J. Marbey, S. Hill, J. Rodriguez-Rivera, H. Nair, M. Gingras, *et al.*, *arXiv preprint arXiv:1912.09448* (2019).
- [53] A. Scheie, M. Sanders, J. Krizan, A. D. Christianson, V. O. Garlea, R. J. Cava, and C. Broholm, *Phys. Rev. B* **98**, 134401 (2018).
- [54] M. J. D. Powell, *The Computer Journal* **7**, 155 (1964).
- [55] F. Gao and L. Han, *Computational Optimization and Applications* **51**, 259 (2012).